SOLPS-ITER modelling of ASDEX Upgrade L-mode detachment states

H. Wu[a], F. Subba[a], M. Wischmeier[b], M. Cavedon[b], R. Zanino[a] and the ASDEX Upgrade Team[b]

[a]NEMO Group, Dipartimento Energia, Politecnico di Torino, Corso Duca degli Abruzzi 24, 10129 Torino, Italy
[b]Max-Planck-Institut für Plasmaphysik, Boltzmannstraße 2, D-85748 Garching, Germany

Abstract:

SOLPS-ITER is used to model ASDEX Upgrade L-mode detachment states including the onset of detachment, the fluctuating detachment, and the complete detachment states, considering drifts and mimicking filamentary convective transport with a radial outward velocity in the low field side. The effect of drifts, perpendicular outward convection and core boundary conditions on the numerical solution is presented. The modelling results are validated against experimental data. We find a good agreement of particle flux at the inner target between modelling results and experimental data. On the opposite, at the outer target computations underestimate measured particle flux by a factor of about 2~3 in the onset of detachment and the fluctuating detachment states.

1. Introduction

SOLPS-ITER [1] currently is the state-of-the-art numerical tool for edge plasma modelling. It includes two modules: the multi-fluid plasma solver B2 [2] for charged species transport in toroidal symmetry, and the Monte Carlo code EIRENE [3], which describes kinetic neutral transport. Compared to the previous SOLPS5.0, the most important features of SOLPS-ITER are the new drifts and currents models [4]. In order to increase confidence on SOLPS-ITER predictive capabilities for future tokamak devices, e.g. ITER [5], DTT [6] and the EU-DEMO [7], it is necessary to validate SOLPS-ITER modelling results, especially for divertor detachment, against experimental data for current tokamak devices, e.g. ASDEX Upgrade (AUG).

Experimental studies [8] showed that in L-mode density ramp discharge, divertor detachment includes three distinct states: the onset detachment state (OS), the fluctuating detachment state (FS) and the complete detachment state (CDS). In the FS, the High Field Side High Density (HFSHD) region, in which the volume electron density n_e is at least a factor of 10 higher than the upstream line averaged density and electron density at targets, has been observed. Previous SOLPS5.0 AUG L-mode modelling results [9] show that, when the inner divertor is detached, the particle flux at the inner target are overestimated by a factor 2~3 and the HFSHD region can be qualitatively reproduced only with the activation of drifts. SOLPS-ITER incorporates many physics/numerics improvements/additions over SOLPS5.0 [10]. The main aim of this work is using SOLPS-ITER to model AUG L-mode three detachment states with such new features. Modelling results are validated against experimental data including: upstream conditions, target conditions, volume electron density in inner divertor and neutral flux density at the dome and pump positions. Similar to previous SOLPS5.0 H-mode modelling [11], we mimic filamentary transport with a radial outward velocity in the low field side of the scrape-off layer.

The rest of the paper is organized as follows: Section 2 describes the experimental discharges that we selected for this study. Section 3 introduces the modelling setup and Section 4 presents the modelling results for three detachment states, comparing them against experimental data. The effect of drifts,

perpendicular outward convective transport and core boundary conditions on the numerical solutions is also presented. In section 5, we presents our conclusions and some perspectives for future work.

2. Experiments

Two AUG L-mode shots: #27100 and #34821 were selected in this study. The two discharges were run in a lower single null configuration with a forward toroidal magnetic field B_t = 2.5 T, and plasma current I_p = 1.0 MA. The $\mathrm{B}\times\nabla\mathrm{B}$ direction pointed towards the lower divertor. Shot #27100 is a density ramp discharge, in which the HFSHD region is observed in the inner divertor volume in the FS and CDS; a more detailed description is presented in [8]. Shot #34821 aims at repeating the three detachment states in #27100 with fixed deuterium fueling rate in each phase under similar discharge conditions. The selected time points with corresponding electron density at the outer mipalne separatrix $n_{e,sep}$ are shown in Table 1 for the different detachment states. Experimental data at such time points are collected over time windows 0.1s width to validate SOLPS-ITER modelling results. For discharge #27100, we ignore changes in the gas puffing level, which are slow compared to the 0.1 s window extension, so that the steady-state assumption is actually an approximation. For shot #34821, the gas puffing rate is constant in the selected time windows so that we have true steady-state in the discharge control parameters. In the FS of the shot #27100, the fluctuation frequency of radiation power near X-point is 5.5 kHz [8]. Measurements also show oscillations of plasma parameters at divertor targets, which means plasma is not truly steady state in the FS. In order to compare experimental data with SOLPS modelling, which produces stationary numerical solutions, the particle fluxes and electron temperature at divertor targets measured by Langmuir probes as described in section 4, are the averaged values within 0.01s. The timescale of 0.01s is two orders of magnitude longer than the timescale of fluctuating radiation ($\frac{1}{5.5\,\mathrm{kHz}} = 2\times10^{-4}\,\mathrm{s}$), thus the measured particle fluxes and electron temperature at divertor targets in discharge #27100 can be approximated by steady signals.

3. Modelling setup

The 96×36 computational grid of SOLPS-ITER is the same as discussed in [10]. Sub-divertor structures, including turbopump, cryopump and neutral baffles equals to those in [11][12] are considered. The albedo for the turbopump surface is 0.92 and for the cryopump is 0.987, giving a pumping speed for the cryopump ~100 m^3/s and ~14m^3/s [11][13] for the turbopump. The kotov-2008 atomic reactions [14] are used in EIRENE for volumetric process. The gas puffing location is at the outer mid-plane. In this study, we could not simultaneously match the experimental gas puffing rate Γ_{puff}, pumping speed Γ_{pump} and electron density at the outer mid-plane separatrix $n_{e,sep}$. Thus, we run SOLPS-ITER in feedback-controlled mode [15][16] for the modelling of three detachment states, in order to exactly reproduce the experimental electron density at the outer mid-plane separatrix $n_{e,sep}$. As mentioned in the introduction, plasma convective transport by filaments is mimicked through a radial outward-directed velocity V_{pinch} applied in the low field side [11]. The perpendicular particle diffusive transport coefficient $D_\perp$, ion and electron heat diffusive transport coefficients $\chi_{\perp i}$ and $\chi_{\perp e}$ for the three detachment states, used everywhere except in private flux region (PFR), are shown in Figure 1. In the PFR, we set constant transport coefficients: $D_\perp$ = 0.4 m^2s^{-1} and $\chi_{\perp i}$ and $\chi_{\perp e}$ = 1.6 m^2s^{-1}. The ballooning scaling ($\propto B^{-1}$) for transport coefficients is considered.

The $E \times B$ and diamagnetic drifts, and all currents (parallel electric current, anomalous current, diamagnetic current, inertial current, ion-neutral current, current due to perpendicular and parallel viscosity, current due to viscosity tensor) are activated in this study. The speed-up scheme of particle flux surface averaging method [17] is used to reduce the CPU running time. Drifts-compatible boundary conditions are used [18]. The input power through the core boundary is estimated to be 0.8 MW, equally distributed between ions and electrons, which is obtained from the experimental measurements of the total heating power minus the radiation power in the main plasma. The particle flux through the core boundary is 5×10^{20}/s to mimic neutrals penetrating deep in the core, ionizing and then coming back towards the plasma edge. Sheath boundary conditions at the targets and leakage wall boundary conditions are also used. The leakage factor value at all wall boundary is 0.01 (the leakage is specified in units of the thermal velocity of electron and ion).

4. Modelling results

4.1 Outer mid-plane profiles

The modelled and measured outer mid-plane profiles of electron density n_e and electron temperature T_e during three detachment states are shown in Figure 2. For electron density n_e, the experimental data are form Integrated Data Analysis (IDA) and edge Thomson Scattering (TS) measurements. In feedback-controlled mode, the electron density at the outer mid-plane separatrix $n_{e,sep}$ is prescribed to exactly match the experimental values. Through adjusting the pinch velocity V_{pinch} and perpendicular diffusion coefficients, especially in the core region near separatrix, there is a reasonable match of n_e outer mid-plane profiles between modelling results and experimental data. For the electron temperature T_e, measurements come from edge Thomson scattering (TS) and Electron Cyclotron Emission (ECE). For the OS and the FS, the modelling results of T_e in the core region near separatrix is ~10% higher than the ECE measurements from #34821 but still within the edge Thomson scattering range of shots #27100 and #34821 which correspond to similar discharge conditions.

In SOLPS-ITER, the total radial particle flux is given by:

$$\begin{aligned}\tilde{\Gamma}_{ay} = \; & (V_{ay}^{(E)} + V_{ay}^{(AN)})n_a + \frac{1}{e}\left(j_y^{(AN)} + j_y^{(in)} + \tilde{j}_y^{(vis\,\parallel)} + \tilde{j}_y^{(vis\perp)} + \tilde{j}_y^{(visq)}\right) \\ & - D_{n,a}\frac{1}{h_x}\frac{\partial n_a}{\partial y} + \tilde{\Gamma}_{ay}^{(dia)}\end{aligned} \tag{0.1}$$

where $V_{ay}^{(E)} n_a$ and $\tilde{\Gamma}_{ay}^{(dia)}$ are the particle fluxes responsible for the $E \times B$ and diamagnetic drifts, $\frac{1}{e}\left(j_y^{(AN)} + j_y^{(in)} + \tilde{j}_y^{(vis\,\parallel)} + \tilde{j}_y^{(vis\perp)} + \tilde{j}_y^{(visq)}\right)$ are the contributions from currents which are only activated in the radial direction where $j_y^{(AN)}$ is the anomalous current, $j_y^{(in)}$ is the inertia current, $\tilde{j}_y^{(vis\,\parallel)}$ is the current driven by parallel viscosity, $\tilde{j}_y^{(vis\perp)}$ is the current driven by perpendicular viscosity and $\tilde{j}_y^{(visq)}$ is the current produced by the components of the viscosity tensor which is connected with the heat. $-D_{n,a}\frac{1}{h_x}\frac{\partial n_a}{\partial y}$ is the diffusive term where $D_{n,a}$ is transport coefficient and $V_{ay}^{(AN)} n_a$ is the convective particle flux which we employ to mimic filaments transport. The profiles of radial particle flux density along the outer mid-plane are presented in Figure 3. For all the three detachment states in our modelling,

the radial particle fluxes due to drifts and currents are much smaller than convection (due to pinch velocity) and diffusion. The convection part are ~1×10^{20} $m^{-2}s^{-1}$, ~4×10^{20} $m^{-2}s^{-1}$ and ~8×10^{20} $m^{-2}s^{-1}$ in the far SOL region for the three detachment states modelling respectively. This is qualitatively consistent with experiments, showing that the particles flux associated to filaments are higher in high density than in low density conditions [19]. For the modelling cases about the FS and CDS, convective transport is dominant in the far SOL region, resulting in an increase of particle flux across wall boundary.

4.2 Target profiles

The modelling results of ion flux Γ_{ion} and electron temperature T_e at the inner and outer targets are compared with Langmuir probe measurements. In order to investigate the effect of drifts close to divertor targets, simulation results without considering drifts, which have the same transport coefficients, gas puffing rate and boundary conditions with drift cases, are also presented. In experiments, in the OS, the inner divertor is partially detached and the outer divertor is in high recycling regime. There is a good agreement of peak value of particle flux at the inner targets (with drift) which is shown in Figure 4(a). While for the ion flux Γ_{ion} at the inner target between Δ5cm ~Δ10cm, the modelling result are lower than the experimental value of #34821 by a factor of 2. A possible explanation is magnetic equilibrium we used in this study which is from discharge #27100. Even if the two discharges have similar plasma conditions, the magnetic equilibria are not exactly the same. The computational grid is also created according to #27100 magnetic equilibrium. These may results in the lower modelling results compared to the experimental data of #34821.

For the peak value of ion flux Γ_{ion} at the outer target in Figure 4(c), the modeling result is lower than experimental data within a factor of ~2. This might be from the gas puffing rate in our modelling which is automatically calculated under the feedback-controlled mode. That value is lower than the experimental value with a factor of ~2. Comparing the modelling result between drifts and without drift cases, it can be found that the drifts change the particle flux profiles at the outer target more than at the inner target. The peak value of particle flux at the outer target is lower by a factor of 2 due to the drifts while at the inner target the drift only moves the peak position from near strike point to ΔS~4cm, not changes the peak value. The drifts increase integrated particle flux Γ_{int} at the inner target about ~40% and decrease at the outer target about 20%.

Electron temperature T_e profiles for the OS modelling are in Figure 4(b) and (d). With drifts, the in-out asymmetry of T_e in experiments is reproduced: the modelled peak value of T_e at the inner target is ~10 eV at ΔS ~ -20 cm, while at the outer target it is ~20 eV close to the strike point. Without drifts, the electron temperature T_e profiles at the inner and outer target are symmetric. We believe that the in-out asymmetry of electron temperature are due to the radial $E \times B$ drift that moves ion from the PFR to the inner divertor region, they then move parallel magnetic field to the inner target and causing a higher electron density near separtrix. The higher density exhibits cooling radiation, causing the formation of the volumetric recombination front in the inner divertor region and ultimately favoring detachment. For the discrepancy of T_e at targets in the far SOL region, this might be due to the constant value of transport coefficient $\chi_{\perp i}$ and $\chi_{\perp e}$ in the SOL region. At the inner target, when ΔS ranges from 0cm to 5cm, the measured Te varies from 1eV to 15eV, which means additional complex physics, e.g. sputtering and kinetic electron effects etc., are involved. However, in our SOLPS-ITER modelling, only the simple sheath boundary condition is applied at the divertor targets. The unconsidered physics in our SOLPS-ITER modelling might be part of the reason why the modelled value are lower than experimentally measurements at the inner target.

For the modelling of FS, there is a good agreement between modelling results and experimental data for ion flux Γ_{ion} profiles at the inner target, as shown in Figure 5(a). As for the ion flux Γ_{ion} at the outer target,

both the total and peak value of modelling results are lower than experimental data by a factor of 3 in Figure 5(c) which is similar to previous SOLPS5.0 study [9]. For discharge #27100, the measured integrated ion flux at the our target is ~15×10^{22} s^{-1} which is higher than the simple Two-Point Model (TPM) scaling value ~6×10^{22} s^{-1} [8]. In this study, SOLPS-ITER modelled value is ~4×10^{22} s^{-1} which is closer to the TPM scaling value. Thus, we believe such discrepancy is caused by some physical mechanisms, which are not included in SOLPS-ITER, such as turbulence. Through comparing modelling results between cases with and without drifts, it can be found that the differences about ion flux at the inner and outer target are within 10%. Recalling to the modelling result of the OS which the drifts decrease the peak value of particle flux at the outer target with a factor ~2, the effect of drifts in the FS are not strong. This is because the $E\times B$ drift is dominant compared the diamagnetic drift. In the FS, the temperature decreases in SOL region that results in the decrease of poloidal and radial electric field, which means the velocity of $E\times B$ decreases.

For electron temperature profiles T_e at the inner target in Figure 5(b), the modeled results are about ~2 eV lower than experimental data especially near strike point, where the measured value is ~15eV. This shows that modelling predicts the inner divertor to be detached, while experiments shows a region attached close to the strike point [8]; this is unlikely to be a measurement error [8] and we cannot explain it at the moment. At the outer target, there is a good agreement of electron temperature as shown in Figure 5(d). In the FS, the inner divertor is detached and the outer divertor is in the high recycling regime. This is successfully reproduced by SOLPS-ITER modelling.

For the CDS, both inner and outer targets are detached in experiments. There is a good agreement of ion flux Γ_{ion} both at the inner and outer targets as shown in Figure 6(a) and (c). Comparing the particle flux with and without drifts, it can be found that the effect of drifts is within 10%. For electron temperature T_e profiles, similar to the modelling of the FS, the modelled electron temperature are lower than experimental data near strike point at both inner and outer target. The modeled electron temperature at the inner target is almost below 2 eV. For outer target, the modelled electron temperature is below 2eV from $\Delta S=0$ to $\Delta S=10$cm. The discrepancy of T_e can be explained by, on the one hand, the uncertainty of Langmuir probes measurements when the temperature is under 3eV, on the other hand, the constant heat transport coefficients in far SOL region similar to the FS modelling. In CDS, both inner and outer target are detached in experiments, the target conditions are reproduced in our modelling.

Based on the modelling of the FS, a parameter scan of electron density at the outer mid-plane $n_{e,sep}$ is performed both with and without drifts, with same modelling setup. First, for the drifts cases, feedback-controlled mode is used to ensure the $n_{e,sep}$ are varied from 1.0×10^{19} m^{-3} to 3.0×10^{19} m^{-3} with 0.1×10^{19} interval. Then the corresponding gas puffing rates are used in no-drift runs, to eliminate the effect due to different deuterium fueling rate. The results are summarized in Figure 7. As the gas puffing rate increase, $n_{e,sep}$ increases similarly both cases with and without drifts. However, for drift cases the density increase is a bit steeper, so that at low puffing rates it is lower than the corresponding without drift runs, and becomes slightly higher at large puff values. The turning point is at a puffing level of 4.35×10^{21} s^{-1} which corresponds to the modelling of FS.

For the integrated ion flux at the inner target Γ_{in}, when considering the drifts, the roll-over occurs when the gas puffing rate is 4.35×10^{21} s^{-1}. Without drifts, the roll-over of integrated ion flux at the inner target Γ_{in} occurs when the gas puffing rate is 5.84×10^{21} s^{-1}. The roll-over of integrated ion flux at the outer target occurs at the same level of gas puffing rate, again 5.84×10^{21} s^{-1}, for both with drifts and without drifts cases. The drifts results in the increase of integrated ion flux at the inner target and decrease outer target before the inner divertor begin to detach. The in-out asymmetry of particle flux are mainly from the effect of radial $E\times B$ drift [20].

For the integrated total power flux at the inner target q_{in}, with drifts the power flux is almost constant at about 0.13MW. For the cases without considering drifts, there is no such trend, and the value is decreased

as the gas puffing rate increases. For the power flux at the outer target, both with drifts cases and without drift cases, it decrease as the increase of gas puffing rate. Without drift, for the pressure drop ratio, which is the ratio of plasma pressure at the targets to plasma pressure at the outer midplane, the value is almost the same at both inner and outer targets. With drifts, the pressure drop ratio at the inner target is obviously lower than the cases without drifts, and the pressure drop ratio at the outer target are higher than the without drift cases. This means the inner target are more detached than outer target and is consistent with the in-out asymmetry of electron temperature in Figure 4.

The radial $E \times B$ drift moves plasma from outer divertor region to PFR and from PFR to inner divertor region. The poloidal $E \times B$ drift transport plasma away inner divertor region and towards outer divertor region [20]. In order to quantitatively analysis the effect of poloidal and radial $E \times B$ drifts, we examine ion flux due to $E \times B$ drift $\Gamma_{E \times B}$ at the inner and outer divertor entrances and interfaces betwen divertor regions and PFR at three different levels of $n_{e,sep}$. The schematic view of the interfaces are shown in Figure 8. Interface 1 is the entrance of inner divertor, interface 2 is the entrance of outer divertor, interface 3 is the interface between PFR and inner diveror region and interface 4 is the interface between PFR and outer diveror region. The results is shown in Figure 9. It can be seen that at low density case, where $n_{e,sep}$ is 1.0×10^{19} m^{-3}, the radial particle flux $\Gamma_{E \times B}$ interfaces 3 and 4 are larger than the poloidal $\Gamma_{E \times B}$ at interfaces 1 and 2 by a factor of 4. Thus, we believe in the high recycling regime, the radial $E \times B$ drift is the main mechanism for the in-out asymmetry of the particle flux. Comparing the distribution of poloidal and radial $E \times B$ drift velocity $V_{E \times B}$ shown in Figure 10(a) and (d), we believe the higher value of radial $\Gamma_{E \times B}$ are due to the high density near separatrix that the poloidal $\Gamma_{E \times B}$ are obviously higher than radial $\Gamma_{E \times B}$ in divertor region.

At medium density case, where $n_{e,sep}$ is 2.0×10^{19} m^{-3}, the radial $\Gamma_{E \times B}$ at interface 3 is higher than the poloidal $\Gamma_{E \times B}$ at interface 1 with a factor of 2. And the radial $\Gamma_{E \times B}$ at interface 4 is 10 times higher than the poloidal value at interface 2. Thus, we believe that the radial $E \times B$ drift is the main reason that results in the reduction of particle flux at the outer target in the FS.

For the high density case, where $n_{e,sep}$ is 3.0×10^{19} m^{-3}, in which the inner target is already detached, the poloidal $\Gamma_{E \times B}$ at interface 1 is higher than the value of radial $\Gamma_{E \times B}$ at interface 3 with a factor of 1.5. Thus, when the inner divertor is detached, poloidal $\Gamma_{E \times B}$ becomes more relevant. For outer divertor region, the situation is similar to the medium density case that the radial $\Gamma_{E \times B}$ is dominant. Comparing the $V_{E \times B}$ distributions between medium density and high density cases in Figure 10 (b), (c), (e) and (f), it can be found that the differences are subtle both in the poloidal and radial directions. Thus, we believe that the different value $\Gamma_{E \times B}$ in Figure 9 are more related to the electron density. A more detailed analysis of the effects of drift, including the diamagnetic contribution, will be presented in the future.

4.3 Electron density in inner divertor volume

The electron density in inner divertor volume is measured along the spectroscopic line-of-sight (LOS) shown in Figure 11 via Stark broadening of the Balmer lines [21]. The different LOS depend on the location of the detectors, and are naturally grouped in bundles named RIV, ZIV, ZON and RXV. The corresponding modeled and measured electron density in the inner divertor volume for the FS and CDS are shown in Figure 12. In order to evaluate the effect of the pinch velocity V_{pinch}, which is assumed to mimic the filamentary transport on the edge plasma, on target profiles and volume electron density, a parameter scan on the pinch velocity V_{pinch} is performed, where we vary it by means of a scaling factor.

Based on the modelling cases of the FS and CDS, the scaling factor about V_{pinch} ranges from 1.0 to 0 with 0.2 interval. When the scaling factor equals to 1, it means the V_{pinch} is the value used in our modelling of the FS and CDS in Figure 3.

For the modelling of fluctuating detachment state, the modelled electron density matches qualitatively the experimental data within a factor of 2, except the value along RIV group. For of the modelled value along RIV group, it can been seen that as the scaling factor increases, the modeled value decreases about ~20% and matches better with experimental data. This is because as the pinch velocity increases, the perpendicular transport at far SOL region is enhanced, resulting in an increase of particle flux across the wall boundary and a decrease of particle flux at both inner and outer target, as shown in Figure 13. As the pinch velocity increases, the peak value of particle fluxes at both inner and outer target are lower by ~25%. The electron temperature at the inner target becomes flat and the position of peak value of Te move far away from strike point due to the enhanced perpendicular transport.

For the modelling of the CDS, the measured electron density along RIV group of LOS is about 5×10^{19} m^{-}, while the modeled value will decrease form ~5.5×10^{20} m^{-3} to ~3.5×10^{20} m^{-3} as the pinch velocity increases. In experiments, the HFSHD front moves along the magnetic lines to above the X-point [8], this characteristic of HFSHD front is not reproduced in our modelling.

4.4 Neutral flux density

Plasma-neutral interactions, which result in momentum and power losses, are important for divertor operation regimes. In order to validate the neutral transport described by SOLPS-ITER, we compare the modelled neutral flux density against measured value at dome and pump positions in Table 2. The position of gauges are the same as in [10]. For the neutral flux density at the dome, it can be see that the discrepancy between modelled and measured values is within ~30%. For the neutral flux density at pump gauge, the modelled value is ~30% higher than experimental value. The lower neutral flux density at the dome and the higher neutral flux density at the pump results in a modelled neutral pressure ratio lower than measured measured by a factor of about 2.

4.5 Core boundary conditions scan

In this study, the input power through the core boundary is 0.8MW, from total heating power minus the radiation power in core, and the particle flux through core boundary is 5×10^{21}/s as mentioned in section 2. For the input power, on the one hand, in SOLPS modelling, the computational grid includes part of core plasma (5 cm), thus the input power cross the core boundary should be higher than 0.8MW. On another hand, due to the error of measurements, the correct input power is not exactly known. For the particle flux through core boundary, in order to be compatible with the new drift models, the value is an estimated one and directly add on the core boundary to mimic neutrals penetrating deep in the core, ionizing and then coming back towards the plasma edge. In order to investigate their effect to the numerical solutions, especially on the ion fluxes at the outer target in the FS, which have a large discrepancy compared with measured value, we performed a core boundary conditions scan including the input power and the particle flux.

Based on the modelling of the FS, the input power is varied from 0.64MW (20% lower) to 0.96MW (20% higher). Figure 14 shows electron density n_e and electron temperature T_e profiles at the outer mid-plane. It can be seen that without any other changes, as the input power increase from 0.64MW to 0.96MW, the electron temperature at the outer mid-plane separatrix increases from 37 eV to 53 eV and the electron density at the outer mid-plane separatrix decreases from $2.16\times10^{21}m^{-3}$ to 1.82×10^{21} m^{-3}. The decrease of

upstream density is to satisfy the parallel momentum balance because the thermal velocity increases due to the higher input power. Figure 15 shows the particle flux Γ_{ion} and electron temperature T_e profiles at the inner and outer targets. For the particle fluxes at the inner target, as input power increases, the particle flux increases. For the particle flux at the outer target, it also increases as input power increases. But, it can been seen, the particle flux profiles expands with lower input power which is not observed at the inner target. This is because as the input power decreases, the outer diver begin to detach from strike point, so that the position of peak value of electron density move away from strike point while the inner divertor is always deteched. For electron temperature profiles at the inner target, even with different input power, they are at same level: 2-3 eV. For the electron temperature at the outer target, as input power increases, the peak value decreases from 12 eV to 6 eV. This means that the outer target are more detached as the power decreases. The reason is that with a lower input power, the electron temperature along flux will be lower that increase the volume recombination which advance the detachment of outer target. Even with 20% higher input power, the peak value of particle flux at the outer target is almost the same. This value is still much lower than the experimental value as presented in Figure 5 (c) (~2×10^{23} $m^{-2}s^{-1}$).

For the scan of particle flux through core boundary, another two value ($1\times10^{20}s^{-1}$ and $1\times10^{21}s^{-1}$) are considered without any other changes. The cases with $1\times10^{20}s^{-1}$ and $1\times10^{21}s^{-1}$ are referred as low paticle flux and high particle flux in the following. The electron density n_e and electron temperature T_e profiles at the outer mid-plane are shown in Figure 16. For the low particle flux case, the electron density at the outer mid-plane separatrix $n_{e,sep}$ is 1.7×10^{19} m^{-3}, for the high particle flux case, the corresponding value is 2.2×10^{19} m^{-3}. For electron temperature profiles, as particle flux across the core boundary increases, the temperature decreases in the core region. In the SOL region, even with different value of particle flux across the core boundary, the electron temperature stays almost unchanged. The particle flux Γ_{ion} and electron temperature T_e profiles at the inner and outer targets are shown in Figure 17, the differences of particle fluxes are within ~5% which means the detached inner target is not sensitive to the particle flux across the core boundary. Even with different value of particle flux across the core boundary, the modelling results of particle flux at the outer target is still lower than the experimental one. In the low particle flux case, the peak value of electron temperature at the outer target is ~10 eV near strike point ($\Delta S \sim 5$cm). In the high particle flux case, the peak value is ~8eV in the far SOL region ($\Delta S \sim 15$cm).

5. Conclusions and perspectives

In this paper we validate SOLPS-ITER on AUG L-mode experimental data, extending a previous work done with SOLPS5.0 on AUG H-mode [11], using a pinch velocity on the low field side to mimic convective filamentary transport. Through adjusting pinch velocity and the perpendicular transport coefficients, the outer mid-plane profiles match well with experimental measurements. The large discrepancy of particle flux at the outer divertor target between modelling result and experimental data in the onset of detachment and the fluctuating detachment states which were already noticed in previous SOLPS5.0 study [9] still exists. For the complete detachment, there is a good agreement between modelling results and experimental data. We analyze the effect of drifts on plasma parameters at the inner and outer targets. It results that drifts are necessary to model the in-out asymmetry of electron temperature at targets in experiments at the onset detachment state. In this case, the $E \times B$ drift increases the ion flux

at the inner target and decreases ion flux at the outer target. In the fluctuating detachment state and the complete detachment state, the effect of drifts on the peak value of the particle flux are within 10%. For the electron density at the inner divertor volume, which is associated with the HFSHD region, the modeled value also match well with experimental data. A parameter scan of pinch velocity shows that as the pinch velocity increases, the inner divertor electron density close to the inner target decreases and slowly approaches the experimental data. The effect of core boundary conditions, including input power and particle flux through core boundary on the numerical solutions are analyzed through parameter scan. Even with different value of input power and particle flux through core boundary, the large discrepancy of ion flux at the outer target in the fluctuating detachment state between measured and modelled value still exists.

In the future, the validated physical model will be applied to the modelling of AUG L-mode impurity seeding detachment focusing on the power load at targets. On a longer term, this could also extend to the analysis of other tokamak devices such as DTT and the EU-DEMO.

Acknowledgements

This work has been carried out within the framework of the EUROfusion Consortium and has received funding from the Euratom research and training programme 2014–2018 and 2019–2020 under grant agreement No. 633053. The views and opinions expressed herein do not necessarily reflect those of the European Commission. The work of HW as a PhD student at Politecnico di Torino, Italy, is supported by the China Scholarship Council (Grant No. 201707820001).

References

[1] S. Wiesen, et al., The new SOLPS-ITER code package, *Journal of nuclear materials* 463 (**2015**): 480-484.
[2] B.J. Braams, A multi-fluid code for simulation of the edge plasma in tokamaks. *NET Report* 68 (**1987**).
[3] D.Reiter, et al., The EIRENE and B2-EIRENE codes, *Fusion science and technology* 47.2 (**2005**): 172-186.
[4] V. Rozhansky, et al., New B2SOLPS5. 2 transport code for H-mode regimes in tokamaks, *Nuclear fusion* 49.2 (**2009**): 025007.
[5] R.A. Pitts, et al., A full tungsten divertor for ITER: Physics issues and design status, *Journal of Nuclear Materials* 438 (**2013**): S48-S56.
[6] R. Albanese, and WPDTT2 Team, DTT: a divertor tokamak test facility for the study of the power exhaust issues in view of DEMO, *Nuclear Fusion* 57.1 (**2016**): 016010.
[7] H. Zohm, et al., On the physics guidelines for a tokamak DEMO, *Nuclear Fusion* 53.7 (**2013**): 073019.
[8] S. Potzel, et al., A new experimental classification of divertor detachment in ASDEX Upgrade, *Nuclear Fusion* 54.1 (**2013**): 013001.
[9] L. Aho-Mantila, et al., Assessment of SOLPS5. 0 divertor solutions with drifts and currents against L-mode experiments in ASDEX Upgrade and JET, *Plasma Physics and Controlled Fusion* 59.3 (**2017**): 035003.
[10] H. Wu, et al., Comparison of SOLPS5. 0 and SOLPS-ITER simulations for ASDEX upgrade L-mode, *Contributions to Plasma Physics* (**2020**).

[11] F. Reimold, et al., The high field side high density region in SOLPS-modeling of nitrogen-seeded H-modes in ASDEX Upgrade, *Nuclear Materials and Energy* 12 (2017): 193-199.
[12] A.V. Chankin, et al., Simulation of ASDEX Upgrade Ohmic plasmas for SOLPS code validation, *Nuclear Fusion* 49.1 (**2008**): 015004.
[13] B. Streibl,et al., In-vessel cryo pump for ASDEX Upgrade divertor II, *Fusion Technology* (1996): 427-430.
[14] V. Kotov, et al., Numerical modelling of high density JET divertor plasma with the SOLPS4. 2 (B2-EIRENE) code, *Plasma physics and controlled fusion* 50.10 (**2008**): 105012.
[15] D.P.Coster, Detachment physics in SOLPS simulations, *Journal of nuclear materials* 415.1 (**2011**): S545-S548.
[16] D.P. Coster, Private communication (**2019**).
[17] E. Kaveeva, et al., Speed-up of SOLPS-ITER code for tokamak edge modeling, Nuclear Fusion 58.12 (2018): 126018.
[18] SOLPS-ITER manual (**2018**).
[19] D. Carralero, et al., On the role of filaments in perpendicular heat transport at the scrape-off layer, *Nuclear Fusion* 58.9 (**2018**): 096015.
[20] A.V. Chankin, et al., Influence of the E×B drift in high recycling divertors on target asymmetries, *Plasma Physics and Controlled Fusion* 57.9 (2015): 095002.
[21] S.Potzel, et al., Electron density determination in the divertor volume of ASDEX Upgrade via Stark broadening of the Balmer lines, *Plasma Physics and Controlled Fusion* 56.2 (**2014**): 025010.

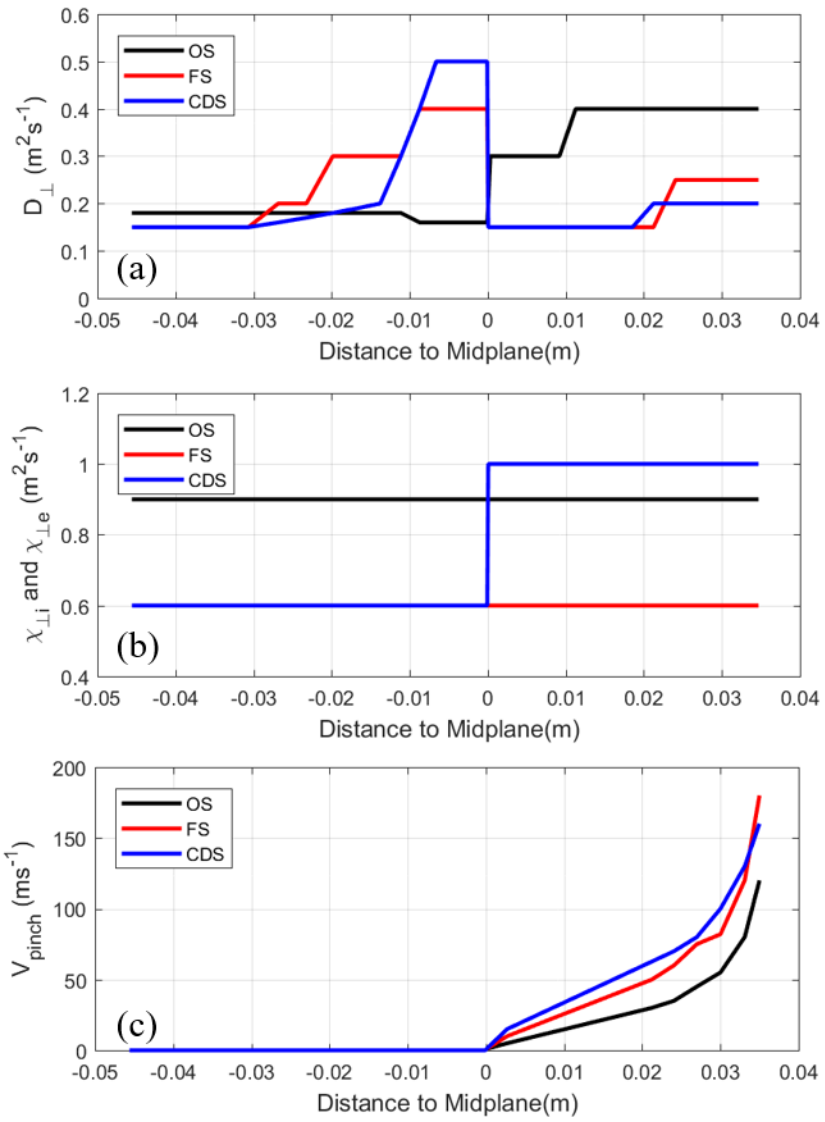

Figure 1. Perpendicular transport coefficients used for the modelling of the onset of detachment (OS), the fluctuating detachment state (FS) and the complete detachment state (CDS). (a) Particle diffusive transport coefficients $D_\perp$, (b) ion and electron heat diffusive transport coefficients $\chi_{\perp i}$ and $\chi_{\perp e}$, and (c) convective pinch velocity V_{pinch}.

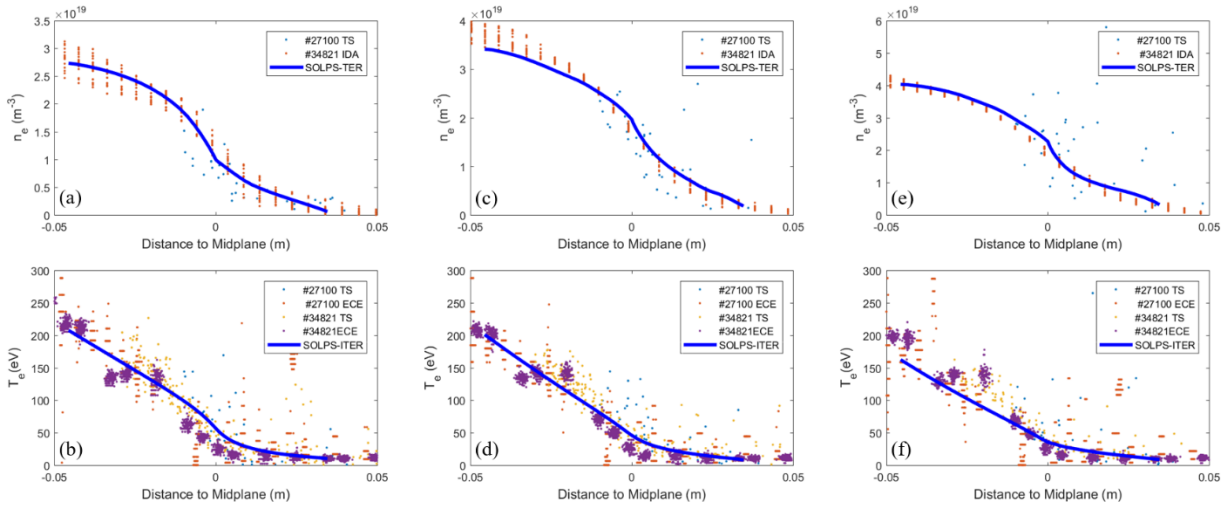

Figure 2. The measured and modeled electron density n_e and temperature T_e profiles at the outer mid-plane. (a) and (b) are for the onset of detachment state, (c) and (d) are for the fluctuating detachment state, (e) and (f) are the complete detachment state. Measured electron density are from Integrated Data Analysis (IDA) and Electron Cyclotron Emission (ECE) diagnostics, electron temperature are from Thomson scattering (TS) and Electron Cyclotron Emission (ECE).

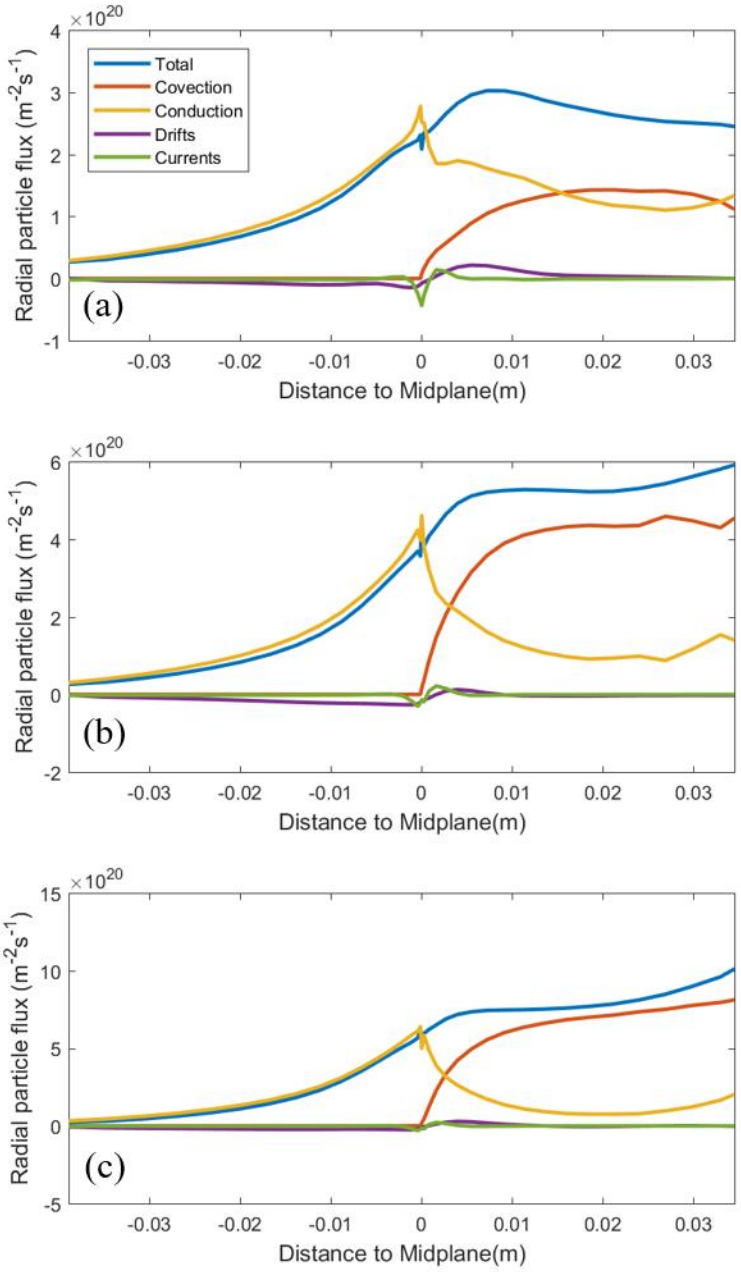

Figure 3. Radial particle flux along the outer mid-plane for (a) the onset of detachment, (b) the fluctuating detachment state and (c) the complete detachment. We show both the total particle flux, and the individual contributions: particle flux due to conduction, particle flux due to convection, particle flux driven by drifts and particle flux due to currents.

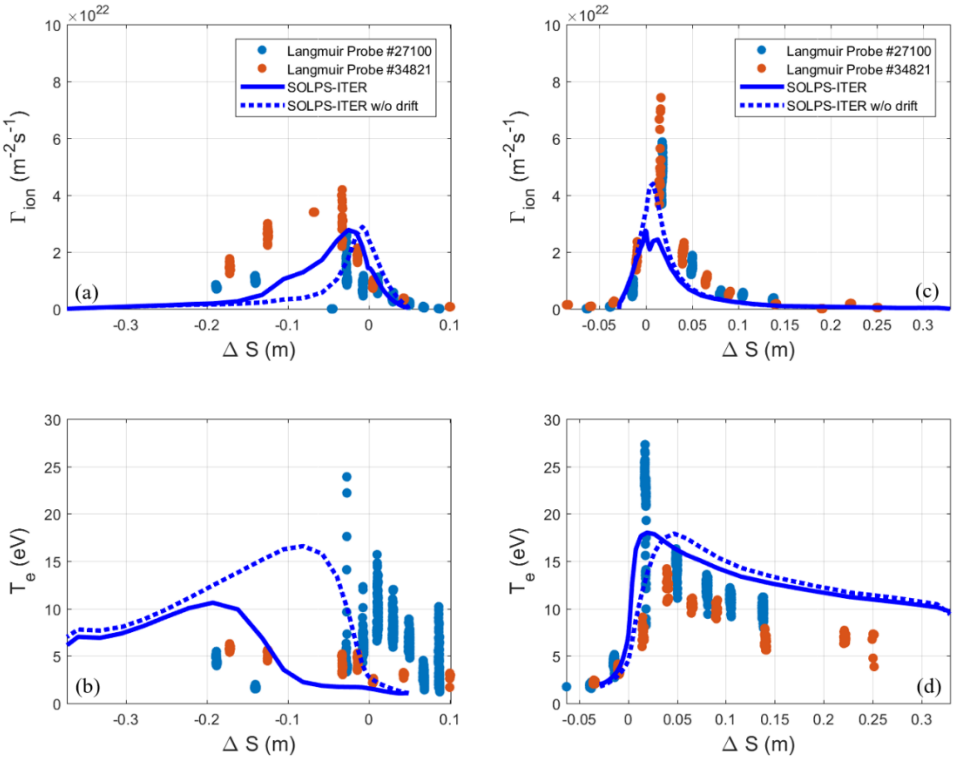

Figure 4. Comparison between measured and modeled value of (a) ion flux Γ_{ion} at the inner target, (b) electron temperature T_e at the inner target, (c) ion flux Γ_{ion} at the outer target, (d) electron temperature T_e at the outer target for onset of detachment. Both discharge #27100 and #34821 are presented. Solid lines are for cases with drifts, and dash lines are for cases without drift.

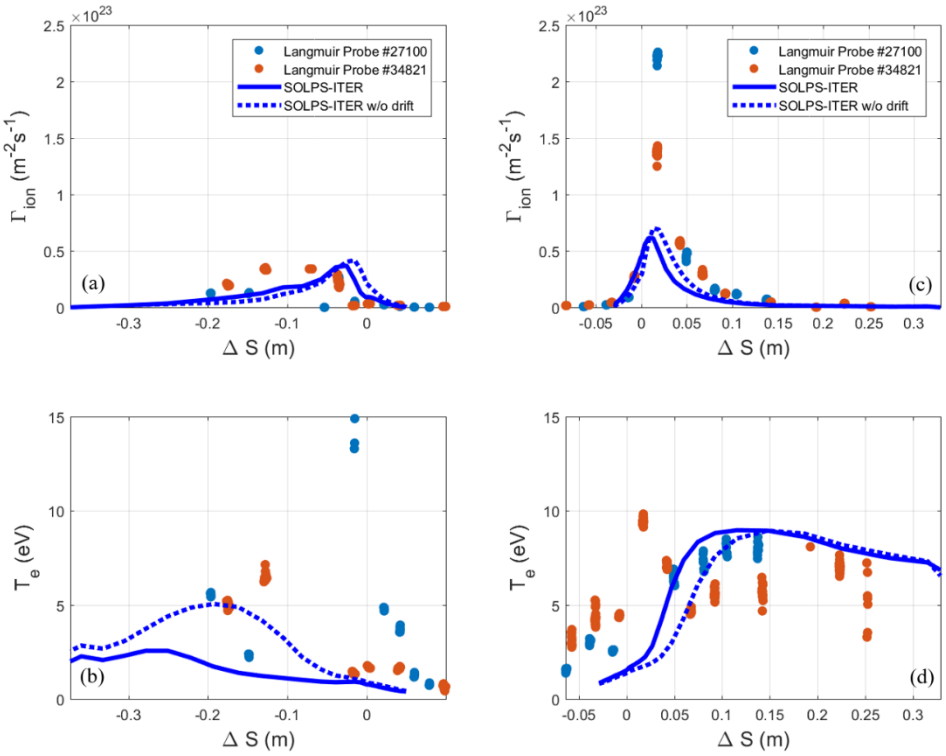

Figure 5. Comparison between measured and modeled value of (a) ion flux Γ_{ion} at the inner target, (b) electron temperature T_e at the inner target, (c) ion flux Γ_{ion} at the outer target, (d) electron temperature T_e at the outer target for the fluctuating detachment state. Both discharge #27100 and #34821 are presented.Solid lines are for cases with drifts, and dash lines are for cases without drift.

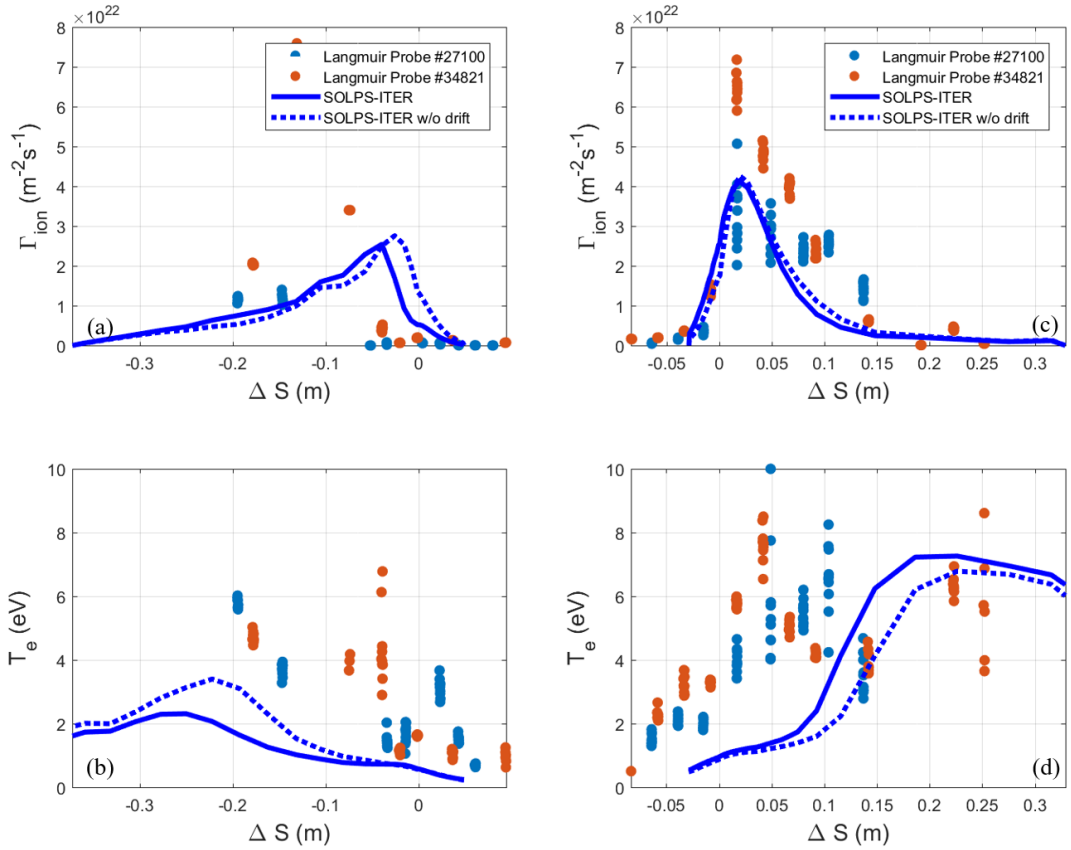

Figure 6. Comparison between measured and modeled value of (a) ion flux Γ_{ion} at the inner target, (b) electron temperature T_e at the inner target, (c) ion flux Γ_{ion} at the outer target, (d) electron temperature T_e at the outer target for the complete detachment state. For experimental data, both discharge #27100 and #34821 are presented. Solid lines are for cases with drifts, and dash lines are for cases without drift.

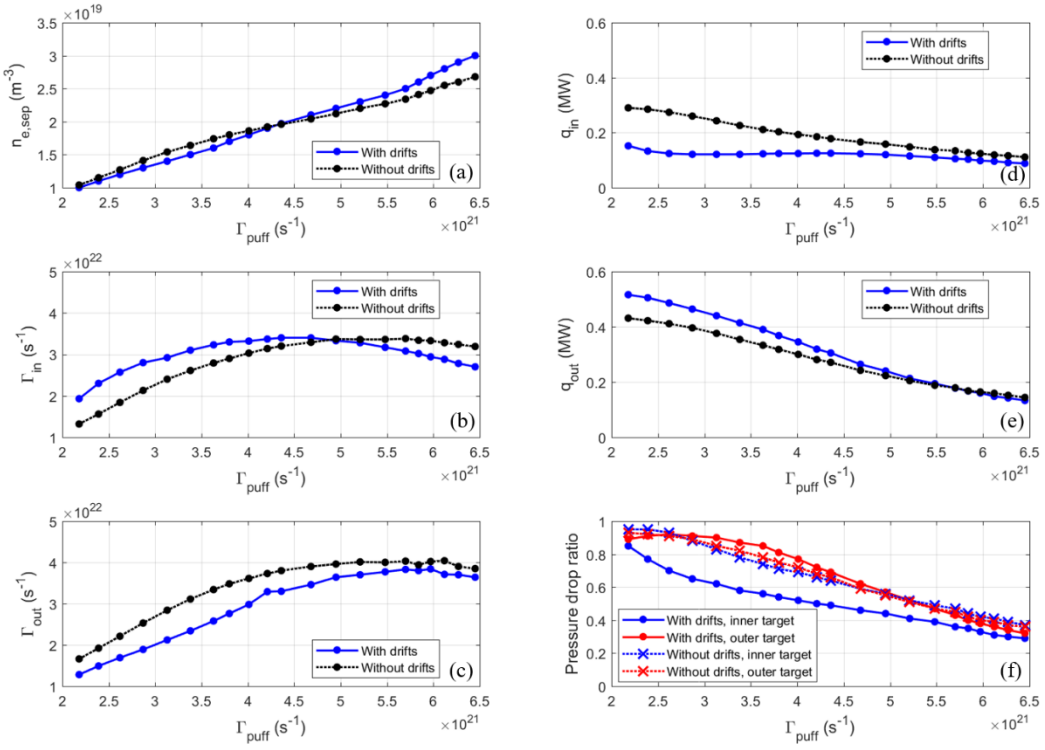

Figure 7. Modelling results about upstream density scan for the electron density at the outer mid-plane separatrix $n_{e,sep}$ based on the modelling of the fluctuating detachment state. (a) $n_{e,sep}$ as a function of gas puffing rate Γ_{puff}, (b) integrated ion flux at the inner target Γ_{in} as a function of Γ_{puff}, (c) integrated ion flux at the outer target Γ_{out} as a function of Γ_{puff}, (d) integrated heat flux at the inner target q_{in} as a function of Γ_{puff}, (e) integrated heat flux at the outer target q_{out} as a function of Γ_{puff}, (f) presurre drop at both inner and outer target as a function of Γ_{puff}. Both with drifts and without drifts cases are presented.

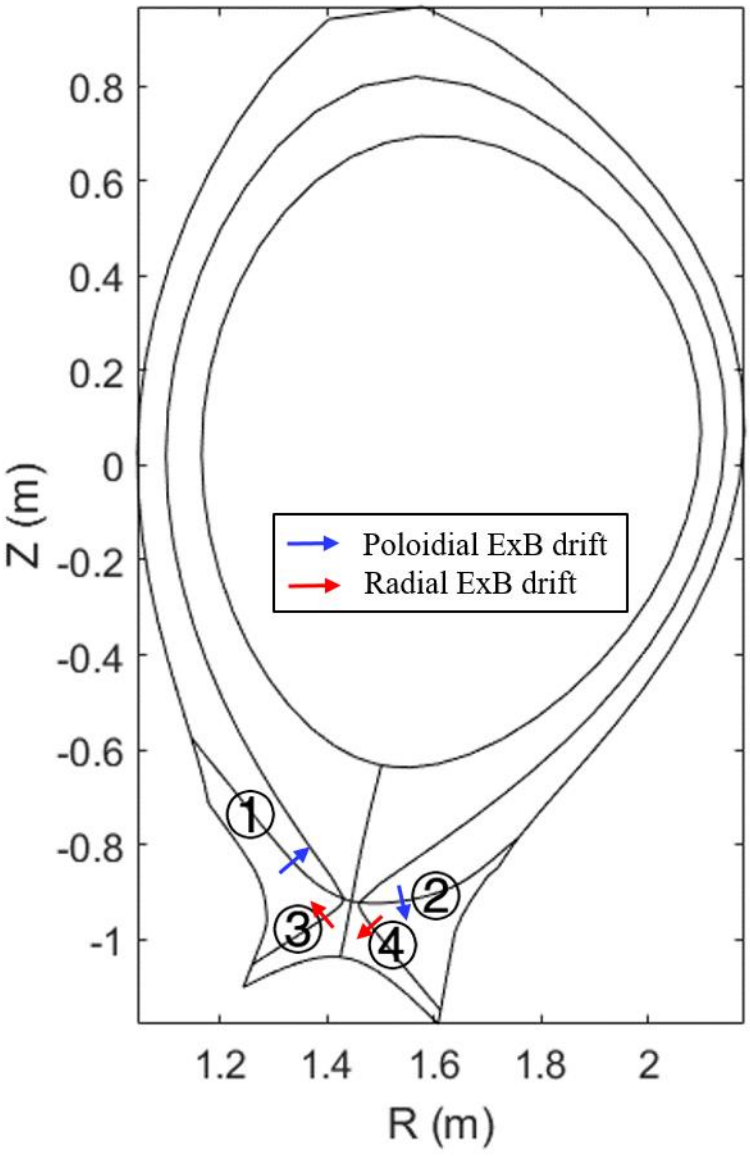

Figure 8. Schematic view of interfaces for poloidal and radial ion flux due to E×B drift. Interface 1 is the entrance of inner divertor, interface 2 is the entrance of outer divertor, interface 3 is the interface between PFR and inner diveror region and interface 4 is the interface between PFR and outer diveror region.

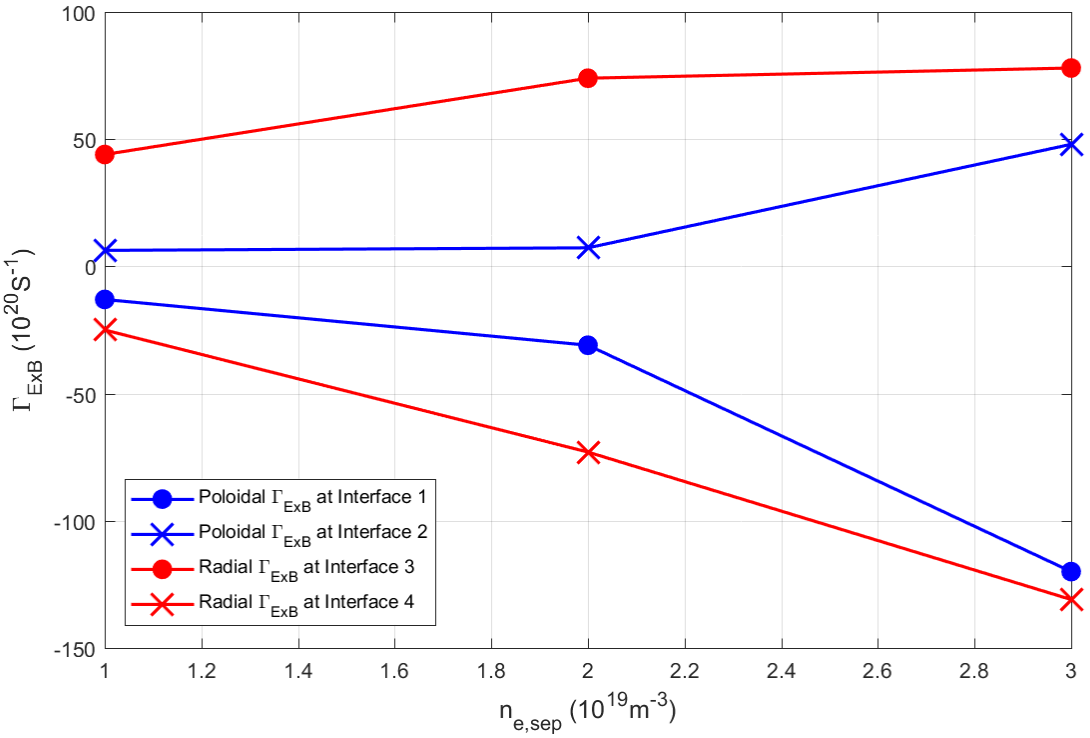

Figure 9. Modelling result of poloidal and radial particle flux due to $E \times B$ drift Γ_{ExB} (10^{20} s^{-1}) across different surfaces with three different electron densities at the mid-plane separatrix $n_{e,sep}$, 1.0×10^{19} m^{-3}, 2.0×10^{19} m^{-3}, and 3.0×10^{19} m^{-3} respectively. The corresponding puffing rates Γ_{puff} are 2.2×10^{21} D/s, 4.7×10^{21} D/s and 6.5×10^{21} D/s respectively. The positive value means particle flux entering divertor region and the negative value means particle flux leaving divertor region.

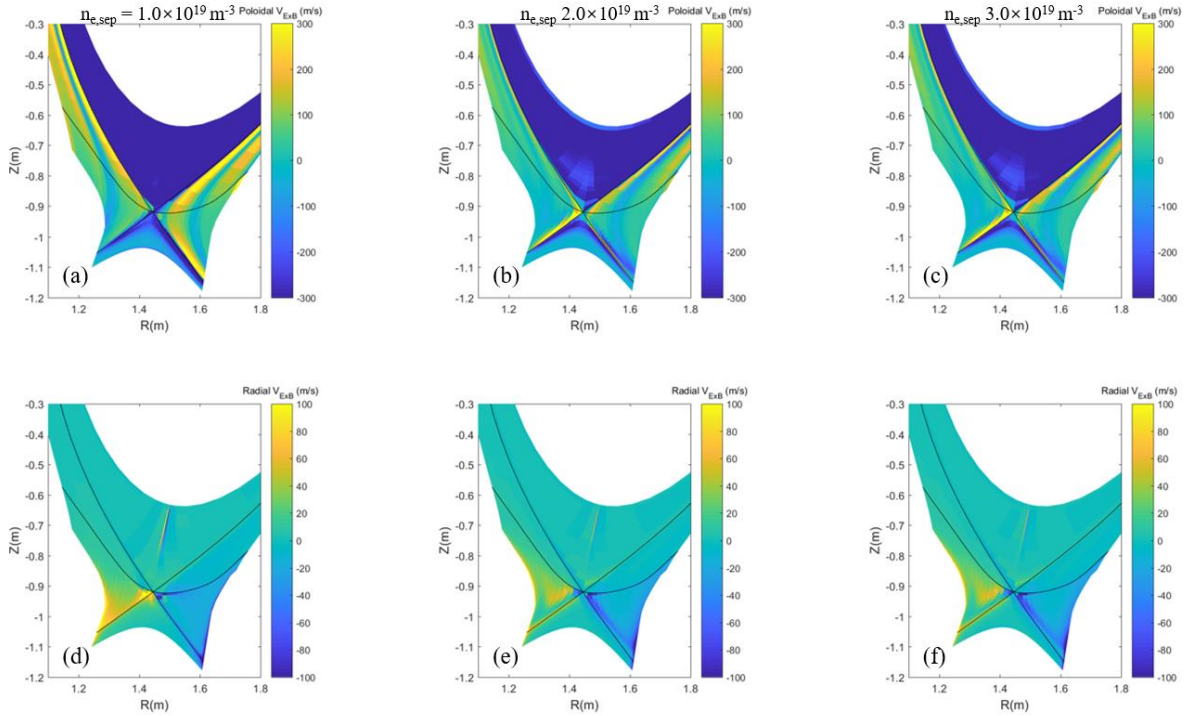

Figure 10. Distribution of poloidal and radial $E \times B$ drift velocity $V_{E\times B}$ at three different midplane electron densities $n_{e,sep}$ = 1.0×10^{19} m^{-3}, 2.0×10^{19} m^{-3}, and 3.0×10^{19} m^{-3} respectively. (a), (b) and (c) are the distribution of poloidal $V_{E\times B}$, (d), (e) and (f) are the distribution of radial $V_{E\times B}$. For poloidal $V_{E\times B}$, positive value means particles are moving from the inner towards the outer target. For radial $V_{E\times B}$, positive value means that particles move away from separatrix towards the far SOL.

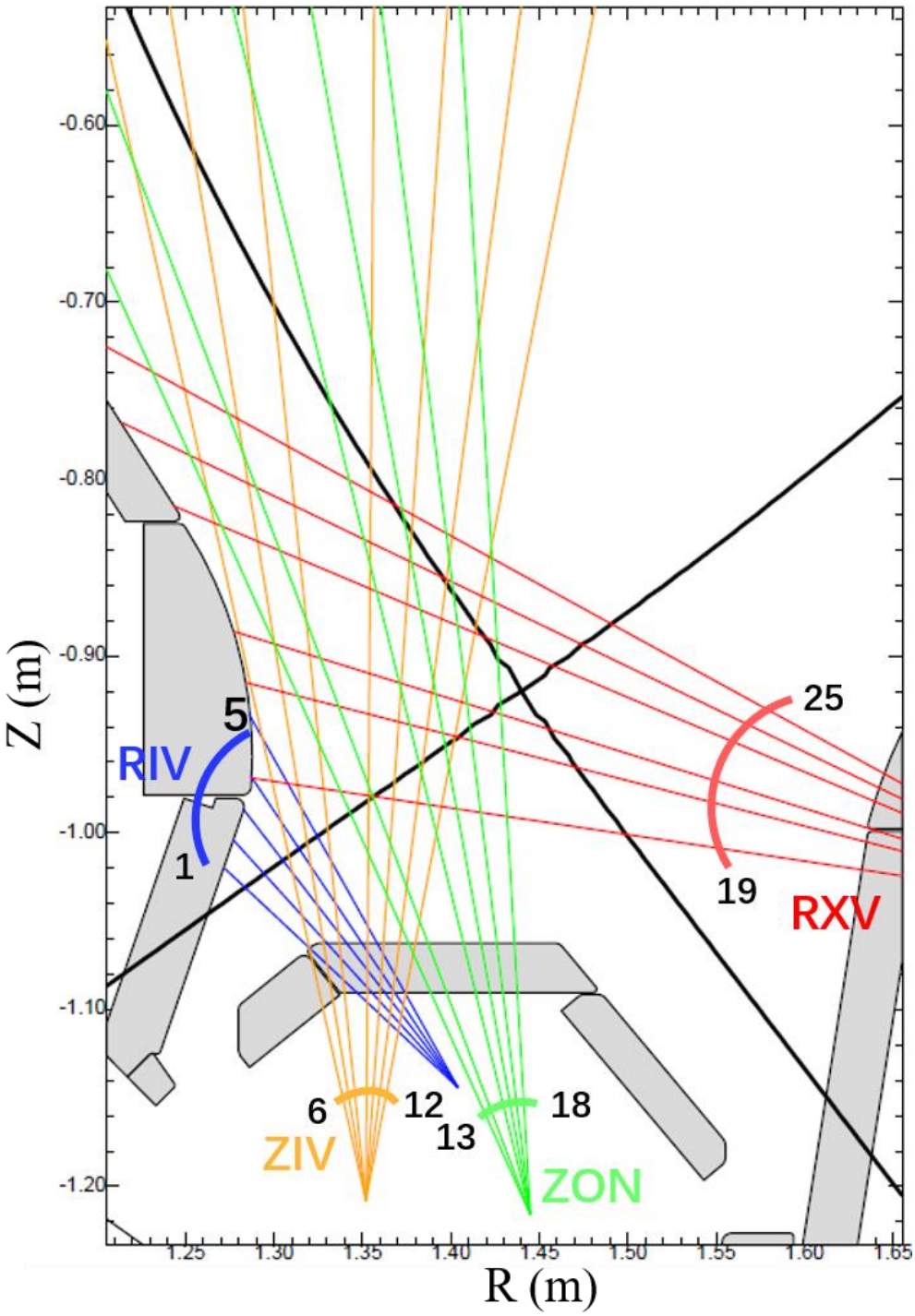

Figure 11. Spectroscopic lines-of-sight (LOS) with index used for measuring the electron density in inner divertor volume.

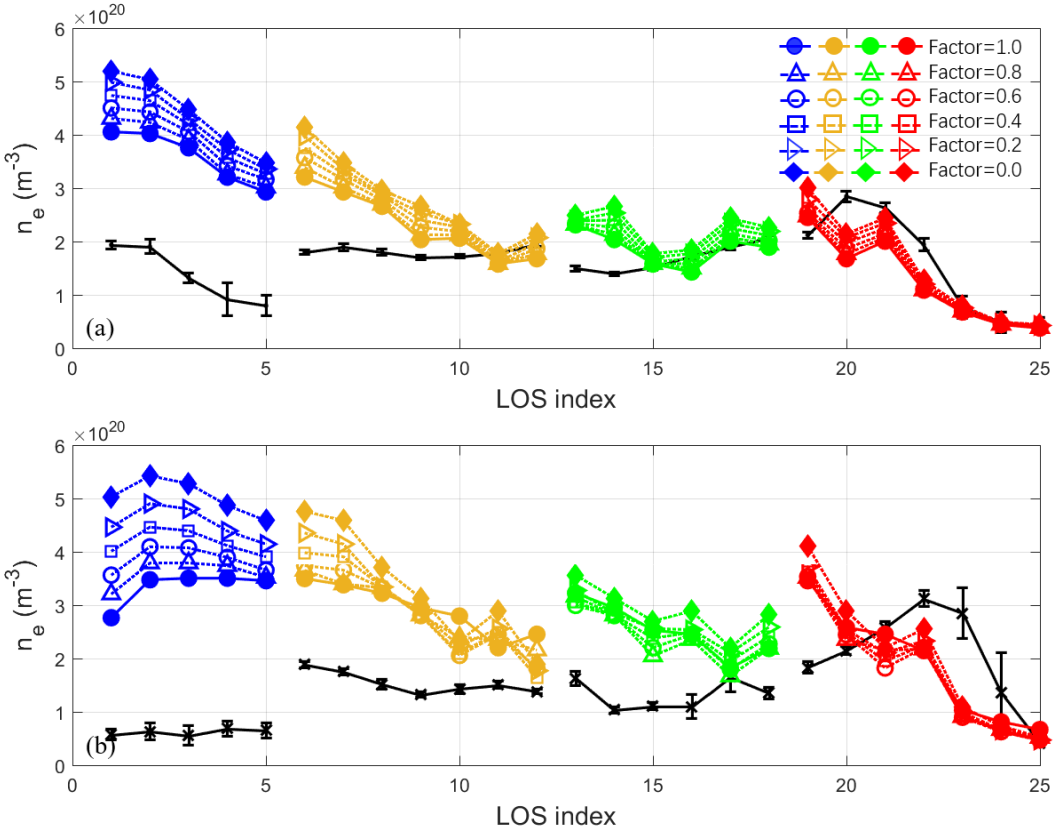

Figure 12. Modelled and measured electron densities $n_{e,inner}$ along LOS for (a) the fluctuating detachment state and (b) the complete detachment state.

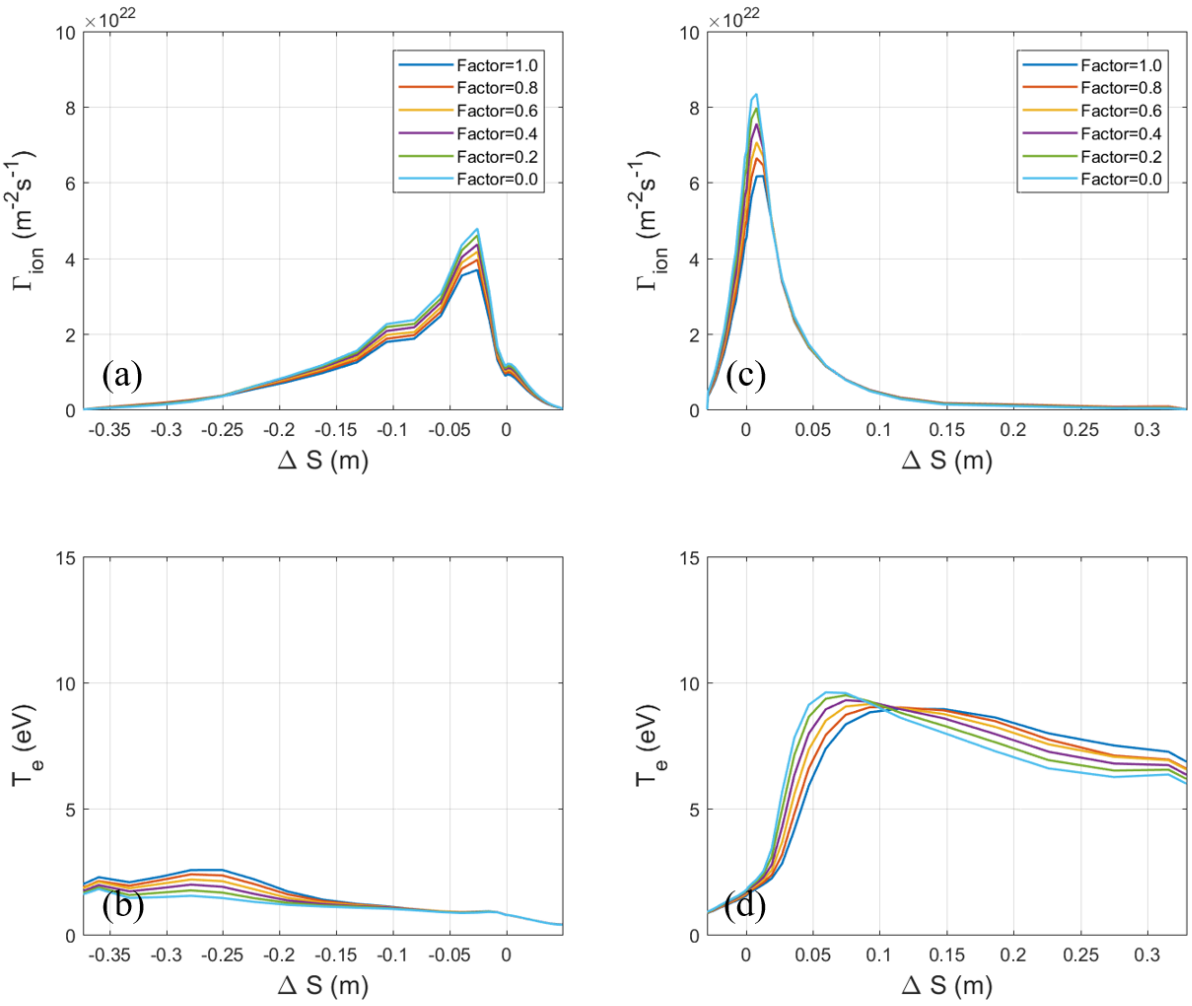

Figure 13. Targets profiles with different pinch velocity based on the modelling of the fluctuating detachment state. (a) Ion flux Γ_{ion} profiles at the inner target, (b) electron temperature T_e profiles at the inner target, (c) ion flux Γ_{ion} profiles at the outer target, (d) electron temperature T_e at the outer target.

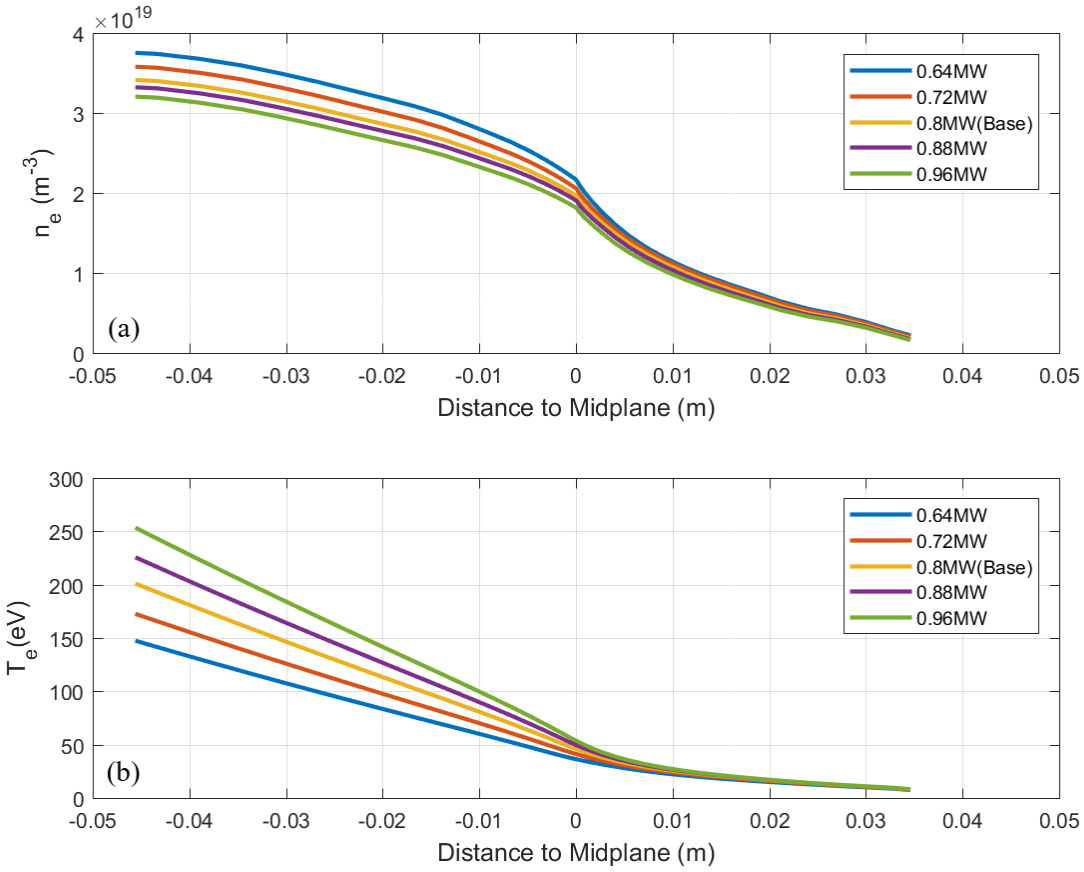

Figure 14. Upstream profiles with different input power based on the modelling of the fluctuating detachment state. (a) Electron density n_e profiles at the outer mid-plane, (b) Electron temperature T_e profiles at the outer mid-plane.

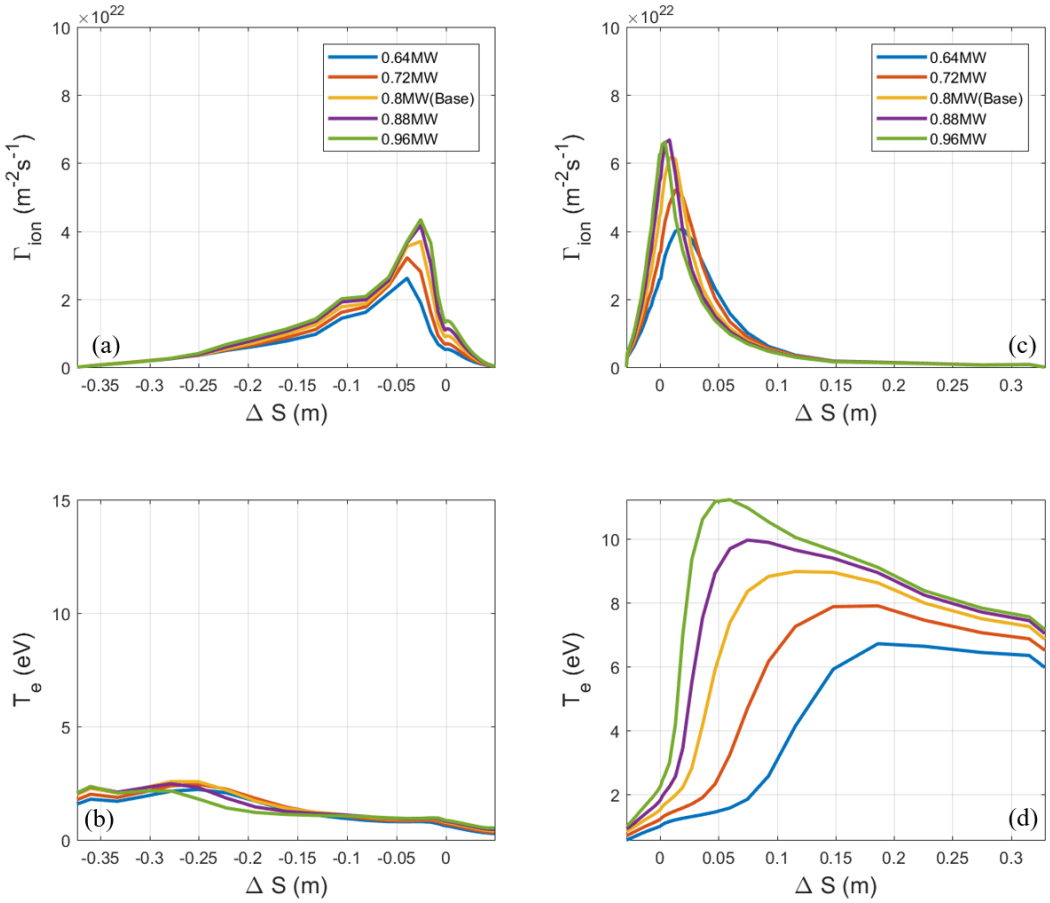

Figure 15. Targets profiles with different input power based on the modelling of the fluctuating detachment state. (a) Ion flux Γ_{ion} profiles at the inner target, (b) electron temperature T_e profiles at the inner target, (c) ion flux Γ_{ion} profiles at the outer target, (d) electron temperature T_e at the outer target.

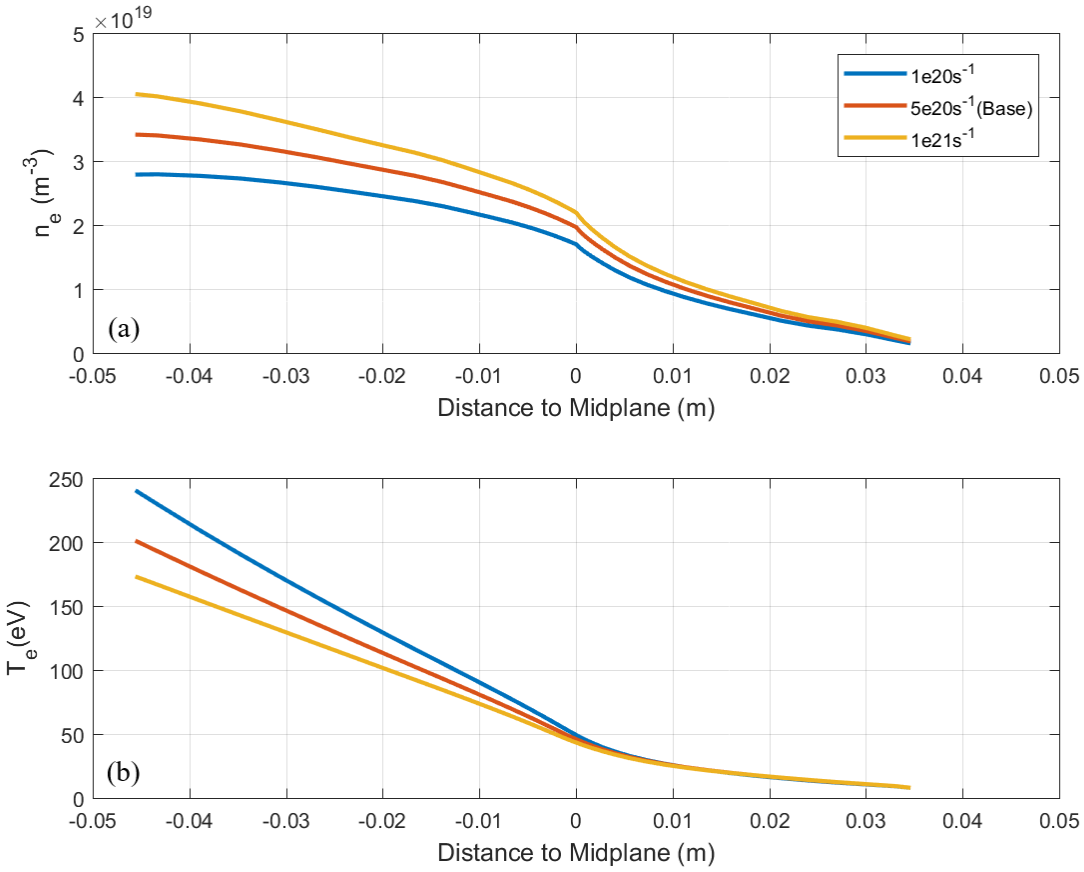

Figure 16. Upstream profiles with different particle fluxes through core boundary based on the modelling of the fluctuating detachment state. (a) Electron density n_e profiles at the outer mid-plane, (b) Electron temperature T_e profiles at the outer mid-plane.

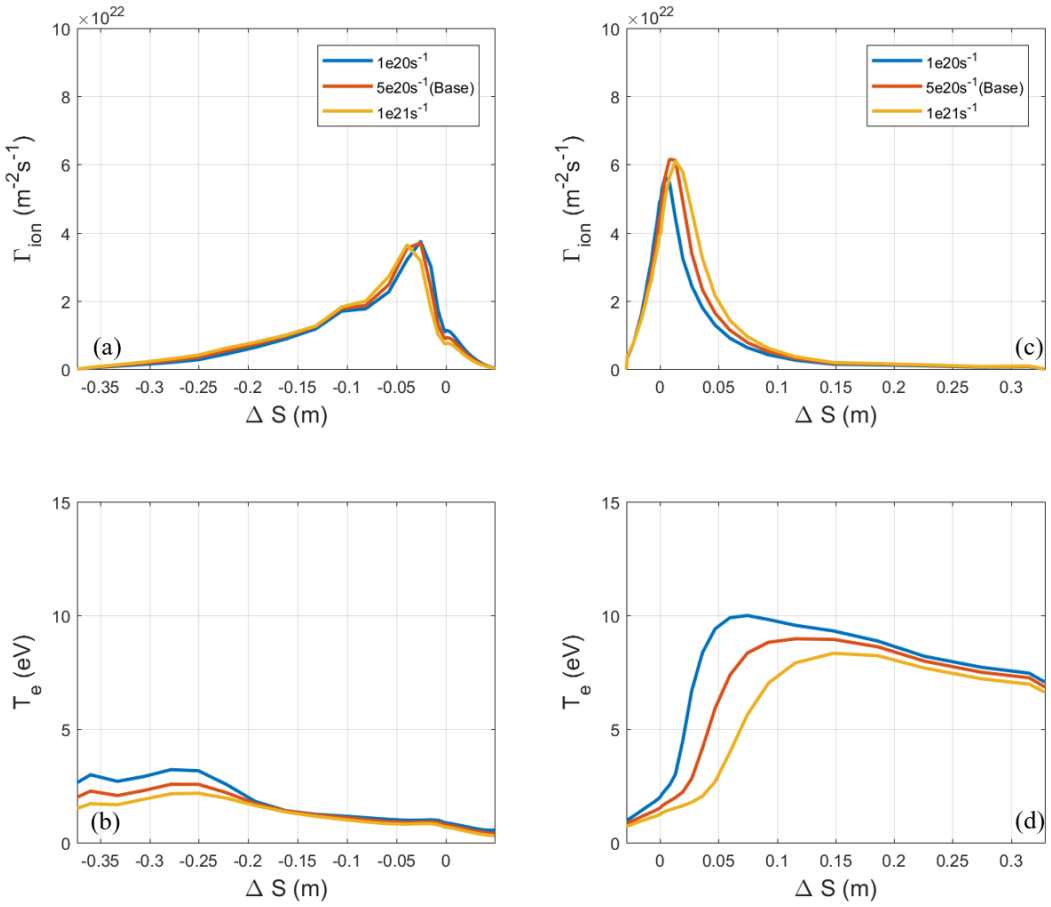

Figure 17. Targets profiles with different particle flux through core boundary based on the modelling of the fluctuating detachment state. (a) Ion flux Γ_{ion} profiles at the inner target, (b) electron temperature T_e profiles at the inner target, (c) ion flux Γ_{ion} profiles at the outer target, (d) electron temperature T_e at the outer target.

Table 1. Divertor detachment states with corresponding electron density at the outer mid-plane separatrix $n_{e,sep}$ and time point for #27100 and #34821. The experimental data at such time points with 0.1s time window are used to validate SOLPS-ITER modelling results.

Divertor detachment states	$n_{e,sep}$ ($\times 10^{19}$ m^{-3})	Time point for #27100	Time point for #34821
Onset of detachment	1.0	2.3s	2.3s
Fluctuating detachment state	2.0	2.8s	2.8s
Complete detachment state	2.2	3.05s	3.2s

Table 2. Measured/ modelled of neutral flux density ($\times 10^{21} m^2/s^{-1}$) at dome and pump locations and the ratio of neutral flux densities at these two position. The experimental data are from discharge #34821. The value at dome are measured by F04 gauge and the value at pump are measured by F05 gauge.

Modelling	Dome	Pump	Ratio
Onset of detachment	18/15	2.0/2.7	9.0/5.6
The fluctuating detachment state	60/45	6.3/7.8	9.5/5.8
The complete detachment state	90/53	7.5/9.8	12.0/5.4